catalysts

MDPI

Article

Integration of CO_2 Adsorbent with Ni-Al_2O_3 Catalysts for Enhanced Methane Production in Carbon Capture and Methanation: Cooperative Interaction of CO_2 Spillover and Heat Exchange

Dong Seop Choi †, Hye Jin Kim †, Jiyull Kim, Hyeona Yu and Ji Bong Joo *

Department of Chemical Engineering, Konkuk University, 120 Neungdong-ro, Gwangjin-gu, Seoul 05029, Republic of Korea; cds1105@konkuk.ac.kr (D.S.C.); jny282592@konkuk.ac.kr (H.J.K.); jiyull0630@konkuk.ac.kr (J.K.); hyeona1014@konkuk.ac.kr (H.Y.)
* Correspondence: jbjoo@konkuk.ac.kr; Tel.: +82-2-450-3545
† These authors contributed equally to this work.

Abstract: In this study, we conducted a comparative analysis of the catalytic behavior of Ni-CaO-Al_2O_3 dual functional material (DFM) and a physical mixture of Ni-Al_2O_3 and CaO-Al_2O_3 in the integrated carbon capture methanation (ICCM) process for promoted methane production. H_2-temperature-programmed surface reaction (H_2-TPSR) analysis revealed that in Ni-CaO-Al_2O_3 DFM, CO_2 adsorbed on the CaO surface can spillover to metallic Ni surface, enabling direct hydrogenation without desorption of CO_2. Ni-CaO-Al_2O_3 DFM exhibited a rapid initial methanation rate due to CO_2 spillover. The Ni-CaO-Al_2O_3 DFM, with Ni and CO_2 adsorption sites in close distance, allows efficient utilization of the heat generated by methanation to desorb strongly adsorbed CO_2, leading to enhanced methane production. Consequently, Ni-CaO-Al_2O_3 DFM produced 1.3 mmol/g_{Ni} of methane at 300 °C, converting 35% of the adsorbed CO_2 to methane.

Keywords: CO_2 capture; methanation; CO_2 adsorbent; dual functional material; integrated carbon capture methanation (ICCM)

Citation: Choi, D.S.; Kim, H.J.; Kim, J.; Yu, H.; Joo, J.B. Integration of CO_2 Adsorbent with Ni-Al_2O_3 Catalysts for Enhanced Methane Production in Carbon Capture and Methanation: Cooperative Interaction of CO_2 Spillover and Heat Exchange. *Catalysts* **2024**, *14*, 834. https://doi.org/10.3390/catal14110834

Academic Editor: Adam F. Lee

Received: 23 September 2024
Revised: 14 November 2024
Accepted: 16 November 2024
Published: 20 November 2024

1. Introduction

The current global phenomena of abnormal climatic conditions and increasing average temperatures can be attributed to the increasing concentration of carbon dioxide in the atmosphere [1]. To address the pressing issue of global climate change, the Paris Agreement of 2015 reached a consensus to limit the increase in global average temperature to below 2 °C above pre-industrial levels. The International Energy Agency (IEA) presents a comprehensive list of technologies and policies to mitigate carbon dioxide emissions within energy-intensive industrial sectors, including steel, cement, oil refining and petrochemicals, with the aim of facilitating the global decarbonization of energy systems by 2070 [2]. As efforts to reduce carbon dioxide emissions, the use of renewable energy and carbon capture and utilization (CCU) technology is an effective strategy in addressing environmental concerns. Active research is being conducted in the field of renewable energy and CCU [3,4]. Renewable energy sources, such as solar and wind power, exhibit more intermittent generation outputs compared to fossil fuel and nuclear power. Therefore, effective energy storage solutions are required to ensure a reliable and consistent supply of renewable energy [5,6]. Power to Gas (P2G) technology presents a promising approach for converting surplus renewable energy that the power grid cannot accommodate into gas, which can then be stored on a large-scale and for the long-term. This technology enables the storage of renewable energy in the form of hydrogen via electrolysis, and it has therefore attracted significant attention for its potential. The utilization of carbon dioxide and renewable energy through the methanation (Sabatier) reaction (Equation (1))

offers the advantage of leveraging existing natural gas infrastructure, thus facilitating immediate use as a fuel source. The carbon dioxide utilized in P2G methanation is derived from widely employed carbon capture processes as well as absorption and adsorption techniques. The carbon dioxide absorption process employs amine-based solutions such as monoethanolamine (MEA) [7,8], while the adsorption process utilizes adsorbents such as alkali metal oxides [9–11] and molecular sieves [12–14]. Both processes require substantial energy for regeneration and additional energy is needed to transport the captured carbon dioxide to the utilization site.

$$CO_2 + 4H_2 \leftrightarrow CH_4 + 2H_2O \quad (1)$$

The integrated carbon capture methanation (ICCM) process is an integrated approach that can address the drawbacks of conventional carbon capture methanation (CCM) technology. Unlike CCM, in which the carbon capture and conversion processes are separate, the ICCM process allows for the sequential occurrence of carbon dioxide adsorption and conversion within a single fixed-bed [15–17] or a circulating fluidized-bed reactor [18], which is due to the presence of the adsorbent and catalyst that are integrated within the reactor. In the CO_2 capture step, the adsorbent selectively captures CO_2 until the adsorption capacity reaches saturation. Subsequently, in the methanation step, the conversion catalyst transforms the carbon dioxide into methane [19–22]. Zongze et al. conducted a techno-economic analysis comparing the CCM process and ICCM [23]. The economic advantage of ICCM can be attributed to the effective heat exchange between CO_2 desorption (endothermic, $\Delta H > 0$) and the methanation reaction (exothermic, $\Delta H < 0$), which has resulted in the price of synthetic natural gas (SNG) gradually coming to approach that of natural gas. L. Chen et al. conducted a conceptual design and assessment of the ICCM process while focusing on its energy consumption and carbon dioxide reduction effects [24]. Their analysis indicates that, when the process is driven by renewable energy sources, the ICCM process demonstrates reduced energy consumption, decreased carbon dioxide conversion costs, and enhanced CO_2 reduction when compared to the conventional CCM process.

Dual functional materials (DFM), which can simultaneously adsorb and convert carbon dioxide, are considered promising candidates for ICCM application. The use of Ru [25–28] and Ni [20,29] metals as conversion materials has been reported. However, Ni exhibits lower methanation activity compared to Ru, and when O_2 is included in the CO_2 stream, the Ni surface can be oxidized, leading to a loss of methanation activity. [30]. Furthermore, as the reduction temperature of nickel metal is higher than that of the methanation reaction, it is difficult to achieve sufficient activation in the H_2 stream that is supplied during the methanation step. Nevertheless, due to the relatively low cost of Ni metal to Ru metal, there is extensive research aiming to overcome its drawbacks in the ICCM reaction [31–33].

Alkali and alkaline earth metal oxides, such as Na [27,34], Mg [29], Ca [19,20], K [35], and Li [15] are commonly used as the adsorptive components in dual functional materials (DFM) for CO_2 capture. M.A. Arellano-Treviño et al. conducted a comparative study examining the performance of DFMs while using Na_2O, CaO, K_2O, and MgO as adsorptive components [30]. In ICCM processes utilizing a model flue gas containing O_2 and H_2O, CaO demonstrated the highest CO_2 capture capacity. Jo et al. investigated the CO_2 capture and methanation activities of Ni/CaO DFM [20]. Their results showed that Ni/CaO DFM exhibited a high CO_2 adsorption capacity of 15.49 mmol/g at 600 °C. During the methanation step, at the same temperature, a substantial amount of methane was produced (14.94 mmol/g). According to a survey of literature, CaO can be considered a suitable adsorbent component for DFM in ICCM process.

L. Falbo et al. and X. Wang et al. investigated the operating mechanism of Ru/Al_2O_3 catalysts in CO_2 methanation [36,37]. They reported that CO_2 reacts with the hydroxyl groups on alumina to form bicarbonate, which subsequently transforms into formate via an interaction with adsorbed hydrogen. The generated formate then rapidly reacts with hydrogen, which is derived from Ru metal, ultimately leading to the formation of adsorbed

CO species. The subsequent hydrogenation of CO results in methane production, where the hydrogenation of CO has been identified as the rate determining step [36]. Li et al. [38] and Jo et al. [39] studied the catalysis mechanism of Ni-CaO based DFMs in ICCM using in situ DRIFTS (Diffuse Reflction Infrared Spectroscopy). During the CO_2 capture step, CO_2 is adsorbed in the form of bicarbonate and carbonate on weak and strong basic sites, respectively. In the methanation step, protons on Ni metal decompose carbonate into formate, which is subsequently converted to CO and then hydrogenated to CH_4 on the metallic Ni surface. Proaño et al. conducted in situ DRIFT studies on Ru-Na_2O-Al_2O_3 DFM and Ru-Al_2O_3 catalyst [40]. They reported that all CO_2 adsorbed on the Ru, Na_2O, and Al_2O_3 surfaces during the CO_2 capture step spilled over to Ru sites with similar behavior during the methanation step. Consequently, the enhanced methanation capacity of DFM compared to Ru-Al_2O_3 catalyst was attributed to its higher CO_2 adsorption capacity. The adsorbent component of dual functional materials (DFM) plays a critical role in transferring the CO_2 that was captured during the CO_2 capture step to the active metal sites during the methanation step.

While there have been numerous studies on ICCM utilizing DFM [41–43], there have also been many cases where adsorbents and catalysts have been used separately. The adsorbents and catalysts can be loaded into reactors in various configuration such as multi-layer [35], double-layer [44], or physically mixed forms [34]. In these cases, the formation of CH_4 has been observed. It is anticipated that the mixture of adsorbents and catalysts will follow a different reaction pathway compared to that which is followed in integrated DFM. The intimate nanoscale interactions, particularly spillover, between the CO_2 adsorbent and methanation catalyst in DFM have been shown to enhance methanation efficiency [45,46]. To further develop ICCM process technology, additional studies that focus on spillover phenomena in DFM and reaction conditions are required.

In this study, Ni and CaO were selected as the active metal and CO_2 adsorbent, respectively. XRD (X-ray diffraction), H_2-TPSR (H_2-temperature-programmed surface reaction) and CO_2-TPD (CO_2-temperature-programmed desorption) analyses of catalysts and adsorbents were conducted. In the ICCM process, the CO_2 capture capacity and methanation activity of five configuration of catalyst bed (Ni-Al_2O_3 catalyst only, Ni-Al_2O_3 + CaO-Al_2O_3 mixture (dual layer, multi-layer, well mixed) and Ni-CaO-Al_2O_3 DFM were compared by using CO_2 stream (50% CO_2/N_2). Specifically, we investigated the process parameter such as reaction temperature of the ICCM process. The optimal reaction conditions for operating parameters and bed material configuration, which are necessary considerations in designing the ICCM process, were proposed. Furthermore, the systematic experimental results were discussed in the context of the results of previously reported studies.

2. Results and Discussion

2.1. Catalyst Characterization

Figure 1 presents the XRD patterns of the adsorbent and catalyst both after calcination and after reduction. The Ni-Al_2O_3 catalyst and Ni-CaO-Al_2O_3 DFM exhibit weak intensity peaks corresponding to NiO (JCPDS #44-1159) approximately $2\theta = 37.2^\circ$ and 43.3° (Figure 1a). In contrast, no peaks corresponding to CaO (JCPDS #01-070-5490) in CaO-Al_2O_3 and Ni-CaO-Al_2O_3 are observed, indicating that the CaO component is dispersed on the support with a crystal size smaller than the XRD detection limit. After reduction of the catalysts at 800 °C in a hydrogen atmosphere (Figure 1b), peaks corresponding to metallic Ni (JCPDS #04-0850) are observed at approximately $2\theta = 44.5^\circ$, 51.8°, and 76.4° in Ni-Al_2O_3 and Ni-CaO-Al_2O_3, while peaks corresponding to CaO remain undetectable. Table 1 presents the textural properties of the adsorbents and catalysts. The N_2 isotherm results show that the loading of Ni and CaO reduces the pore volume and specific surface area, implying that Ni and CaO are both loaded inside the pores. Ni-CaO-Al_2O_3, with 10 wt% loading of both Ni and CaO, exhibits the smallest specific surface area and pore volume among all samples. The H_2-pulse chemisorption test was conducted to measure

the dispersion and surface area of the metallic Ni after reduction at 800 °C. The dispersion and surface area of metallic Ni in Ni-Al_2O_3 are 1.45% and 0.78 m^2/g, respectively, which are higher than those of Ni-CaO-Al_2O_3, i.e., 0.17% and 0.13 m^2/g, respectively. This difference can be attributed to the preparation process of Ni-CaO-Al_2O_3 catalyst, in which CaO is impregnated after Ni, thereby partially covering the metallic Ni surface and in turn hindering the access of probe molecules onto the Ni metal [47].

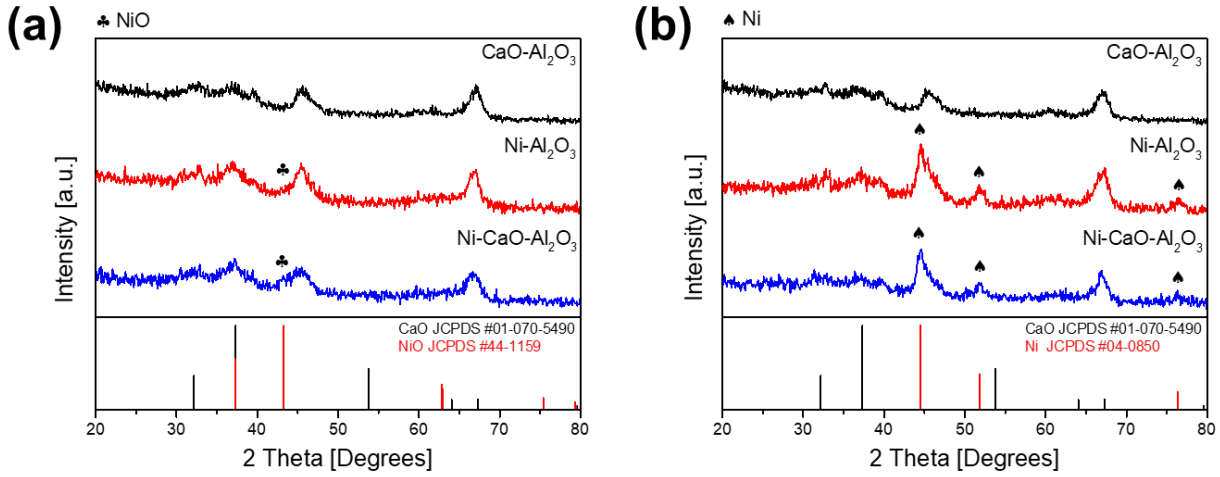

Figure 1. XRD (X-ray diffraction) patterns of catalyst and adsorbent (**a**) after calcination and (**b**) after reduction.

Table 1. Texture properties of catalysts and adsorbents.

	Ni Crystalline Size [nm] [a]	Specific Surface Area [m^2/g] [b]	Pore Volume [cm^3/g] [b]	Ni Contents [wt%] [c]	CaO Contents [wt%] [c]	Ni Dispersion [%] [d]	Ni Surface Area [m^2/g_{Cat}] [d]
Al_2O_3	-	151.7	0.46	-	-	-	-
Ni-Al_2O_3	7.36	127.9	0.37	8.01	-	1.45	0.78
CaO-Al_2O_3	-	112.4	0.36	-	8.73	-	-
Ni-CaO-Al_2O_3	6.30	89.7	0.28	11.36	10.00	0.17	0.13

[a] Calculated by the Scherrer equation based on (200) face of Ni. [b] Characterized by N_2 physisorption. [c] Characterized by ICP-OES (inductively coupled plasma optical emission spectrometry). [d] Characterized by H_2-pulse chemisorption.

Figure 2 and Table 2 present the CO_2-TPD profiles of each sample. The Al_2O_3 support and the Ni-Al_2O_3 catalyst, without CaO, exhibit CO_2 adsorption capacities of 0.166 and 0.178 mmol/g, respectively, thus showing a minimal difference. This indicates that the presence of Ni has a negligible impact on CO_2 adsorption capacity. It should be noted that the metallic Ni surface can serve as a CO_2 adsorption site, and CO_2 dissociates upon adsorption on the metallic Ni surface as $CO_{(ad)}$ and $O_{(ad)}$ [39,48–50]. Nevertheless, the introduction of Ni appears to have a negligible impact on the CO_2 adsorption capacity due to the low dispersion and surface area of metallic Ni in Ni-Al_2O_3. Al_2O_3 and Ni-Al_2O_3 exhibit two CO_2 desorption peaks approximately 100 °C and 500 °C. The peak observed at lower temperatures is associated with the desorption of the physically adsorbed CO_2 and decomposition of bicarbonate that is formed between surface OH groups and CO_2 [51] whereas the peak at higher temperatures corresponds to the decomposition of more stable carbonate species [52]. The introduction of CaO to Al_2O_3 and Ni-Al_2O_3 significantly increases the CO_2 adsorption capacity. Notably, the amount of CO_2 desorbed below 400 °C was shown to increase by more than threefold. The enhanced weak basic sites observed in CaO-Al_2O_3 and Ni-CaO-Al_2O_3 correspond to the decomposition of carbonate species formed between CaO and CO_2.

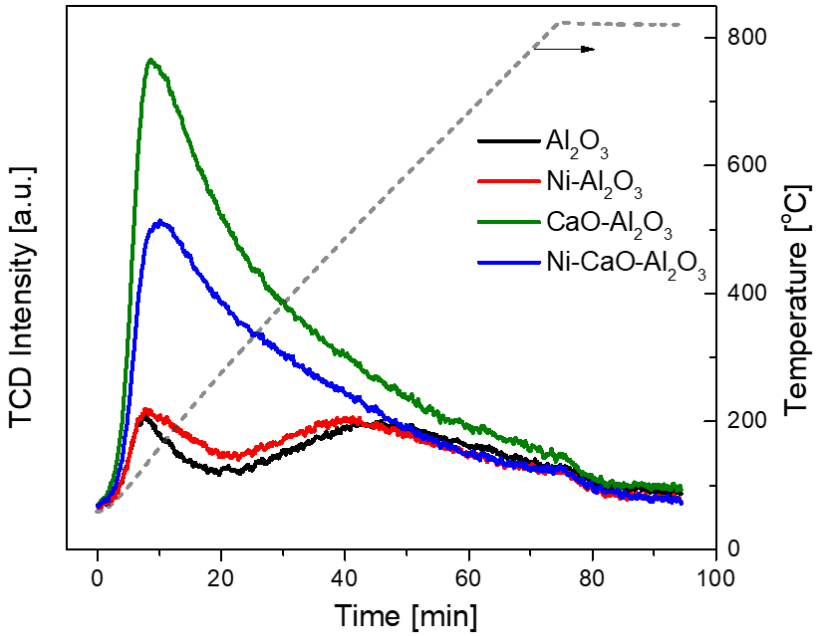

Figure 2. CO_2-TPD (CO_2-temperature-programmed desorption) profiles of catalysts and adsorbents (the dotted line represents the temperature of samples).

Table 2. CO_2-TPD results of catalysts and adsorbents.

	Weak Basicity [mmol CO_2/g] [a]	Strong Basicity [mmol CO_2/g] [b]	Total Basicity [mmol CO_2/g]	Utilization Efficiency [%] [c]
Al_2O_3	0.052	0.114	0.166	-
Ni-Al_2O_3	0.069	0.109	0.178	-
CaO-Al_2O_3	0.319	0.184	0.503	22.58
Ni-CaO-Al_2O_3	0.214	0.130	0.344	10.31

[a] Determined by the amount of desorbed CO_2 below 400 °C. [b] Determined by the amount of desorbed CO_2 above 400 °C. [c] Mole of CO_2 desorbed per mole of CaO, CO_2/CaO.

Since Al_2O_3 and Ni-Al_2O_3 are also capable of adsorbing a significant amount of CO_2, the CO_2 adsorption capacity that is attributable to CaO was determined by subtracting the CO_2 adsorption capacities of Al_2O_3 and Ni-Al_2O_3 from those of CaO-Al_2O_3 and Ni-CaO-Al_2O_3, respectively. The CO_2 adsorption capacities attributable to CaO in the CaO-Al_2O_3 adsorbent and Ni-CaO-Al_2O_3 DFM were found to be 0.35 and 0.18 mmol/g_{CaO}, respectively. Assuming that CO_2 is adsorbed on CaO in a 1:1 molar ratio, the utilization efficiencies of CaO (Table 2) was found to be 22.58% and 10.31% for CaO-Al_2O_3 and Ni-CaO-Al_2O_3, respectively, with both being lower than 100%. The utilization efficiency of CaO, which reflects the dispersion of CaO, indicates that CaO is less exposed on the surface in Ni-CaO-Al_2O_3 compared to CaO-Al_2O_3. Ni-CaO-Al_2O_3, with 10 wt% loading of both Ni and CaO, has a lower specific surface area and pore volume compared to CaO-Al_2O_3 (Table 1). Based on the CO_2-TPD results, it is expected that using catalysts and adsorbents separately would be more advantageous for CO_2 capture capacity in ICCM than the use of DFM.

Figure 3 presents the H_2-TPSR results after reduction at 800 °C along with CO_2 capture at 300 °C. To assess H_2-TPSR based on the integration of the CaO and Ni, Al_2O_3 was mixed to ensure that the Ni and CaO contents in each sample mixture were uniformly maintained at 5 wt%. The peaks observed in H_2-TPSR can result from hydrogen consumption, CO_2 desorption, and the formation of CO and CH_4. In the case of CaO-Al_2O_3, peaks are observed in the range of 300–500 °C, and these correspond to the decomposition and/or hydrogenation of the carbonate species that are identified in the CO_2-TPD analysis (Equations (2) and (3)) [53]. For Ni-Al_2O_3, peaks are observed at a lower temperature range (200–400 °C). Due to the pre-reduction at 800 °C, hydrogen consumption as a result of the

reduction of NiO is negligible. Considering that CO_2 capture occurs at 300 °C, the peaks observed at temperatures below 300 °C can be attributed to the hydrogenation of adsorbed CO_2 species rather than CO_2 desorption. Meanwhile, the relatively low signal intensity of Ni-Al_2O_3 is due to its low CO_2 adsorption capacity, as confirmed by the CO_2-TPD results (Figure 2).

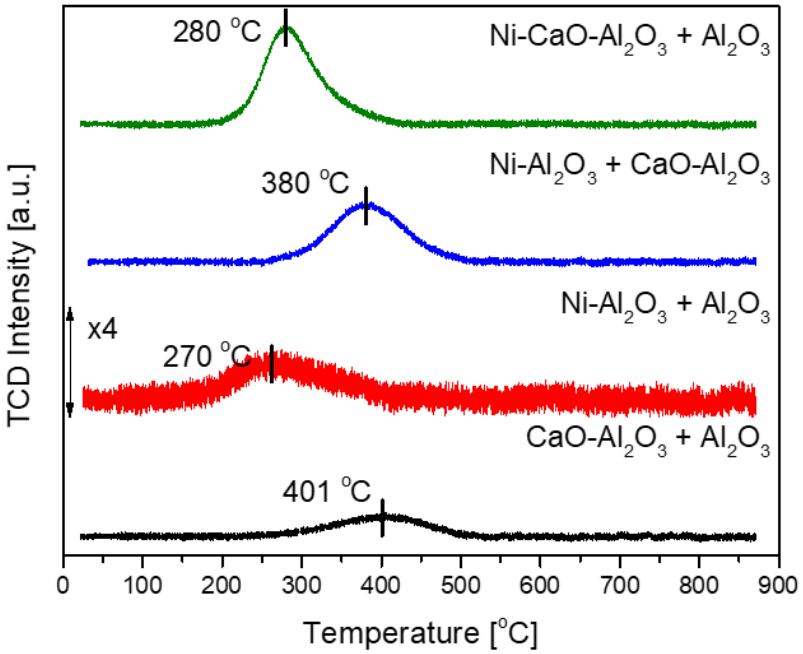

Figure 3. H_2-TPSR (H_2-temperature-programmed surface reaction) profiles of adsorbents and catalysts mixture.

When Ni and CaO are supported on separate supports (Ni-Al_2O_3 + CaO-Al_2O_3), the H_2-TPSR profile resembles that of CaO-Al_2O_3. Peaks are formed in the temperature range of approximately 300–500 °C, with an observed increase in peak intensity compared to CaO-Al_2O_3. The increased peak intensity can be attributed to the greater amount of hydrogen consumption due to the hydrogenation reaction facilitated by the metallic Ni surface of Ni-Al_2O_3. Considering that the peak formation in CaO-Al_2O_3 is due to the decomposition and hydrogenation of adsorbed carbonate species, the hydrogenation reaction pathway in the mixture of Ni-Al_2O_3 and CaO-Al_2O_3 can be described using the following reaction equations: The adsorbed CO_2 on the surface of CaO in CaO-Al_2O_3 is desorbed (Equation (2)) and/or hydrogenated (Equation (3)). The CO_2 and/or CO derived from CaO-Al_2O_3 react with hydrogen on the metallic Ni surface of Ni-Al_2O_3 to produce CH_4 (Equations (4) and (5)).

Route 1:

$$CaO...CO_{2(ad)} \leftrightarrow CaO + CO_2 \quad (2)$$

$$CaO...CO_{2(ad)} + H_2 \leftrightarrow CaO + CO + H_2O \quad (3)$$

$$CO + 3H_2 \leftrightarrow CH_4 + H_2O \quad (4)$$

$$CO_2 + 4H_2 \leftrightarrow CH_4 + 2H_2O \quad (5)$$

In contrast, when Ni and CaO are integrated on the same support (Ni-CaO-Al_2O_3 + Al_2O_3), the H_2-TPSR profile is similar to that of Ni-Al_2O_3, with the formation of peaks observed at a lower temperature range (200–400 °C). The peaks observed below 300 °C can be attributed to the direct hydrogenation of carbonate species formed on the adsorbent (CaO) by metallic Ni. Unlike the hydrogenation reaction pathway that is observed in Ni-Al_2O_3 + CaO-Al_2O_3, the hydrogenation reaction pathway in Ni-CaO-Al_2O_3 DFM is proposed to proceed via both Route 1 and Route 2.

Route 2:

$$Ni + 4H_2 + CaO...CO_{2(ad)} \leftrightarrow Ni + CaO + CH_4 + 2H_2O \quad (6)$$

$$Ni + H_2 + CaO...CO_{2(ad)} \leftrightarrow Ni + CaO + CO + H_2O \quad (7)$$

Since the self-decomposition of adsorbed carbonate species occurs above 300 °C, the peak formation below 300 °C can be attributed to the hydrogenation of carbonate species (Route 2: Equations (6) and (7)). In the proposed route 2, the adsorbed carbonate species spillover to the metallic Ni, followed by sequential hydrogenation to form CH_4 or CO [46,54,55]. At temperatures above 300 °C, the self-decomposition of the adsorbed carbonate species can occur, followed by the hydrogenation of CO_2 and/or CO (Route 1). Considering that the peak center of Ni-CaO-Al_2O_3 is located at 280 °C, the reaction pathway of hydrogenation via carbonate species spillover is dominant in Ni-CaO-Al_2O_3 DFM. Compared to Ni-Al_2O_3, the enhanced peak intensity in Ni-CaO-Al_2O_3 can be attributed to the significant improvement achieved in CO_2 capture capacity with the introduction of CaO. The H_2-TPSR results confirm that both Ni-Al_2O_3 + CaO-Al_2O_3 mixtures and Ni-CaO-Al_2O_3 DFM are capable of CO_2 capture and in situ methanation. It was also observed that the methanation process follows distinct reaction pathways depending on the integration of Ni and CaO.

2.2. The Catalyst Activity Test: Direct Methanation

Figure 4 illustrates the thermodynamic equilibrium results calculated by the HSC Chemistry software program. The thermodynamic equilibrium was determined based on the stoichiometric composition of CO_2 direct methanation with an H_2/CO_2 ratio of 4. The equilibrium composition of the products (Figure 4a,b) varies between the high temperature and low temperature regions. In the low-temperature region, which is below 300 °C, the exothermic CO_2 direct methanation reaction (Equation (1)) predominates, resulting in the primary formation of CH_4 and H_2O. Meanwhile, in the high-temperature region, above 400 °C, CO formation begins as a result of the reverse water-gas shift reaction (Equation (8)). In this high-temperature region, the exothermic CO_2 direct methanation reaction becomes thermodynamically less favorable, whereas the endothermic reverse water-gas shift reaction becomes more favorable. Especially, at temperatures above 600 °C, the reverse water-gas shift reaction is the predominant process. Consequently, as the temperature increases in the high-temperature region, the yield of CH_4, which is a product of CO_2 methanation, decreases while the formation of CO increases.

$$H_2 + CO_2 \leftrightarrow H_2 + H_2O \quad (8)$$

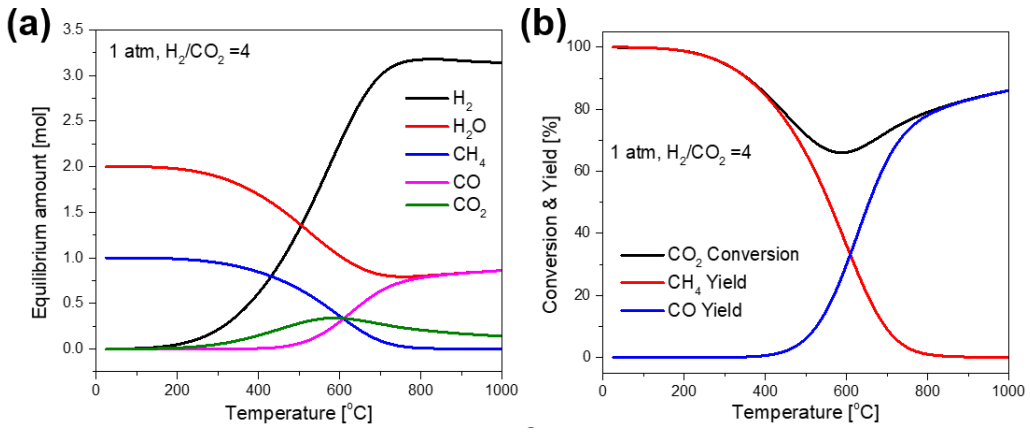

Figure 4. Thermodynamic equilibrium analysis results of the CO_2 methanation reaction: (**a**) product equilibrium amount and (**b**) equilibrium CO_2 conversion and product yield.

Figure 5a–c depicts the results of CO_2 direct methanation over Ni-Al_2O_3, a Ni-Al_2O_3 + CaO-Al_2O_3 mixture, and Ni-CaO-Al_2O_3 DFM. While these results do not directly represent the performance in ICCM, they provide insights into catalytic activity during CO_2 direct methanation and the distribution of potential products in the temperature range from 200–600 °C. Al_2O_3 was mixed to ensure that there would be consistent catalyst bed volume and content of Ni and CaO within the catalyst bed. The activities of both Al_2O_3 and CaO-Al_2O_3 were found to be negligible, with CO_2 conversion rates below 0% in the low-temperature region (200–300 °C) and less than 10% even in the high-temperature region above 500 °C. No CH_4 formation was observed with Al_2O_3 and CaO-Al_2O_3 across all temperature ranges, and only trace amounts of CO were detected above 300 °C. These observations suggest that only metallic Ni is catalytically active in the methanation reaction, and that the formation of CO can be attributed to either the reverse water-gas shift reaction or the hydrogenation of carbonate species, as observed in the H_2-TPSR of CaO-Al_2O_3 [56]. No significant differences in catalytic activity were observed among the Ni-Al_2O_3, Ni-Al_2O_3 + CaO-Al_2O_3, and Ni-CaO-Al_2O_3 samples. During CO_2 direct methanation, no substantial interaction was observed between Ni and CaO when they were integrated or supported separately on Al_2O_3 particles.

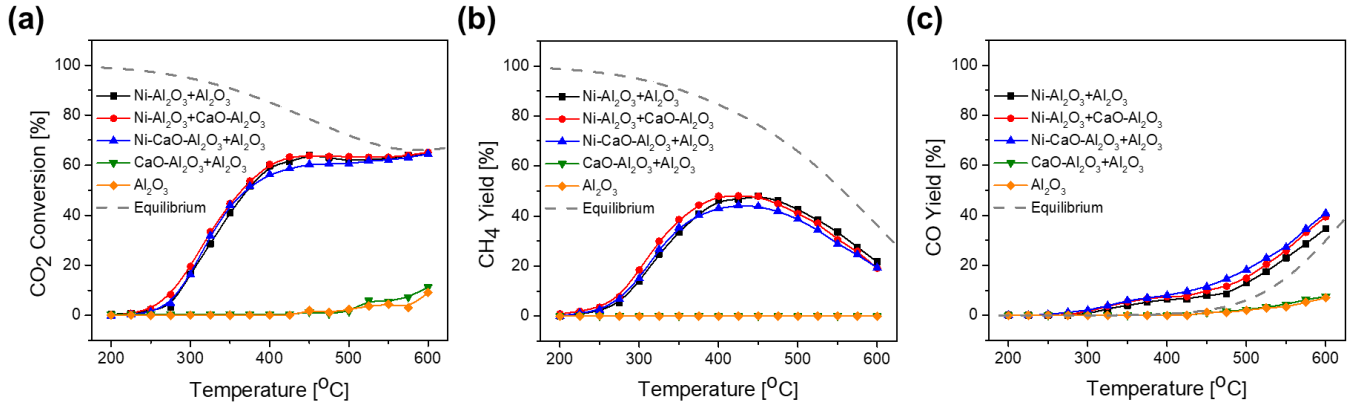

Figure 5. The effect of temperature on CO_2 methanation: (**a**) CO_2 conversion, (**b**) CH_4 yield, and (**c**) CO yield, with thermodynamic equilibrium shown as gray dashed lines.

2.3. The Catalyst Activity Test: Integrated Carbon Capture Methanation (ICCM)

Figure 6 depicts the setup used for an investigation into the catalytic activity of several catalyst bed configuration in a fixed-bed integrated carbon capture methanation (ICCM) system. Figure 6a shows the catalyst bed configuration that was designed to investigate the interaction between Ni and CaO in ICCM. The contents of Ni, which are an active component for methanation; CaO, as a CO_2 adsorbent; and Al_2O_3 were kept constant in the catalyst bed. Figure 6b shows the CO_2 capture capacity, CH_4 production, and CO_2 desorption amount in various catalyst bed configurations. The ICCM process was conducted sequentially through CO_2 capture step (10 min), purge step (10 min) and methanation step (40 min). The measured CO_2 adsorption capacity during CO_2 capture step does not distinguish between physical adsorption and chemical adsorption of CO_2. It should be noted that the measured CO_2 adsorption capacity may be slightly overestimated due to the possibility of weakly physisorbed CO_2 being desorbed during the subsequent purge step. No CO formation was observed during the ICCM test. In the CO_2 capture step, the CO_2 capture capacity followed the order of Ni-Al_2O_3 + CaO-Al_2O_3 (dual layer, multi-layer, well mixed) > Ni-CaO-Al_2O_3 DFM > Ni-Al_2O_3. These results are consistent with the results of CO_2-TPD (Figure 2, Table 2). CaO-Al_2O_3 has a large specific surface area and pore volume, and the utilization efficiency of CaO is higher than that of Ni-CaO-Al_2O_3. However, there was a different trend for methane production in the methanation step, which was in the order of DFM > well mixed > multi-layer > dual layer > catalyst only. This indicates that the physical distance between Ni and CaO plays a crucial role in the methanation

of adsorbed CO_2. As suggested by H_2-TPSR (Figure 4), CO_2 spillover is inhibited in the Ni-Al_2O_3 + CaO-Al_2O_3 mixture due to the physical isolation of Ni and CaO on separate Al_2O_3 particles. Therefore, CH_4 formation occurs through a series of steps, including CO_2 desorption from CaO, diffusion to Ni-Al_2O_3 particles in gas phase, adsorption on Ni-Al_2O_3 particles, and subsequent hydrogenation over metallic Ni surface. The desorption of CO_2 from CaO-Al_2O_3 is an endothermic process, and it requires an external heat supply. It should be noted that the ICCM test was conducted under isothermal conditions, with the same temperature used for both the CO_2 capture and methanation steps, unlike the H_2-TPSR test. Heat transfer to CaO-Al_2O_3 originates from the CO_2 methanation (exothermic reaction, $\Delta H < 0$) occurring on the metallic Ni surface over Ni-Al_2O_3. The results presented in CO_2-TPD (Figure 2) and the ICCM results of Ni-Al_2O_3 (Figure 6b) as well as CO_2 adsorption and conversion are also observed on Ni-Al_2O_3. These findings indicates that heat exchange between Ni and CaO is required to induce more methanation. The order of methane formation, DFM > well mixed > multi-layer > dual layer, correlates with the shorter average distance between Ni and CaO. Ni-CaO-Al_2O_3 DFM, despite its relatively low CO_2 adsorption capacity, can effectively utilize the captured CO_2 since the adsorption and conversion sites are supported on a single particle, which enables efficient heat transfer to CaO. As a result, the conversion of captured CO_2 follows the order of DFM > well mixed > multi-layer > dual layer > catalyst only (Figure 6c). Figure 6d,e shows the methane production profiles over time during the methanation step. Ni-CaO-Al_2O_3 shows a much faster initial methane production rate than the Ni-Al_2O_3 + CaO-Al_2O_3 mixture. In Ni-CaO-Al_2O_3, Ni and CaO are integrated on a single support, so adsorbed CO_2 can more easily receive heat generated from metallic Ni and facilitate the utilization of more thermally stable carbonate species, resulting in faster methane production. On the other hand, in the Ni-Al_2O_3 + CaO-Al_2O_3 mixture, the long distance between Ni and CaO reduces the heat exchange efficiency between Ni and CaO. As a result, the desorption rate of adsorbed CO_2 is decreased, which slows down the methane production rate.

Figure 7 shows the ICCM results of DFM in the temperature range of 250–350 °C. The CO_2 capture capacity decreases continuously as the reaction temperature increases. CO_2 adsorption is known to be an exothermic process that is less favored at high temperatures. On the other hand, the CH_4 production tends to increase as the temperature increases. According to the results of thermodynamic equilibrium analysis (Figure 4) and direct methanation (Figure 5), the methanation reaction (Equation (1)) is dominant and controlled by kinetics in the temperature range between 250 °C and 350 °C. This leads to an increase in the conversion of captured CO_2 (Figure 7b).

Figure 8 presents a schematic diagram illustrating the proposed reaction pathway based on the preceding catalyst characterization and methanation experimental results. In the CO_2 capture step, the majority of CO_2 adsorbs on the surface of CaO in the form of carbonate species in both Ni-Al_2O_3 + CaO-Al_2O_3 mixtures and Ni-CaO-Al_2O_3 DFM, while a minor portion adsorbs as bicarbonate species on the hydroxyl groups of the Al_2O_3 support. When Ni and CaO are isolated on different supports (Figure 8a), the small amount of CO_2 adsorbed on Ni-Al_2O_3 undergoes spillover to the metallic Ni surface, after which it reacts with hydride species on the metallic Ni surface to form CH_4. Prior to methanation over Ni-Al_2O_3, desorption of CO_2 adsorbed on CaO-Al_2O_3 does not occur. A small amount of CO_2 adsorbed on Ni-Al_2O_3 undergoes conversion, and the generated heat is transferred to neighboring Ni-Al_2O_3 or CaO-Al_2O_3 particles, inducing desorption of CO_2. The desorbed CO_2 undergoes gas-phase diffusion toward adjacent Ni-Al_2O_3 particles, subsequently adsorbing onto the hydroxyl groups of the Al_2O_3 surface, supplying the CO_2 required for methanation. In contrast, in Ni-CaO-Al_2O_3 (Figure 8b), where Ni and CaO are integrated onto a single support, CO_2 adsorbed on both the CaO and Al_2O_3 surface can be transferred to the metallic Ni surface via spillover, inducing a significant amount of methanation. The heat that is generated in this process is effectively transferred to adsorption sites that are located near the reaction site, and this process can also induce the decomposition of

thermally stable carbonates. As a result, a very rapid initial methane formation rate and high CO_2 conversion rate are observed.

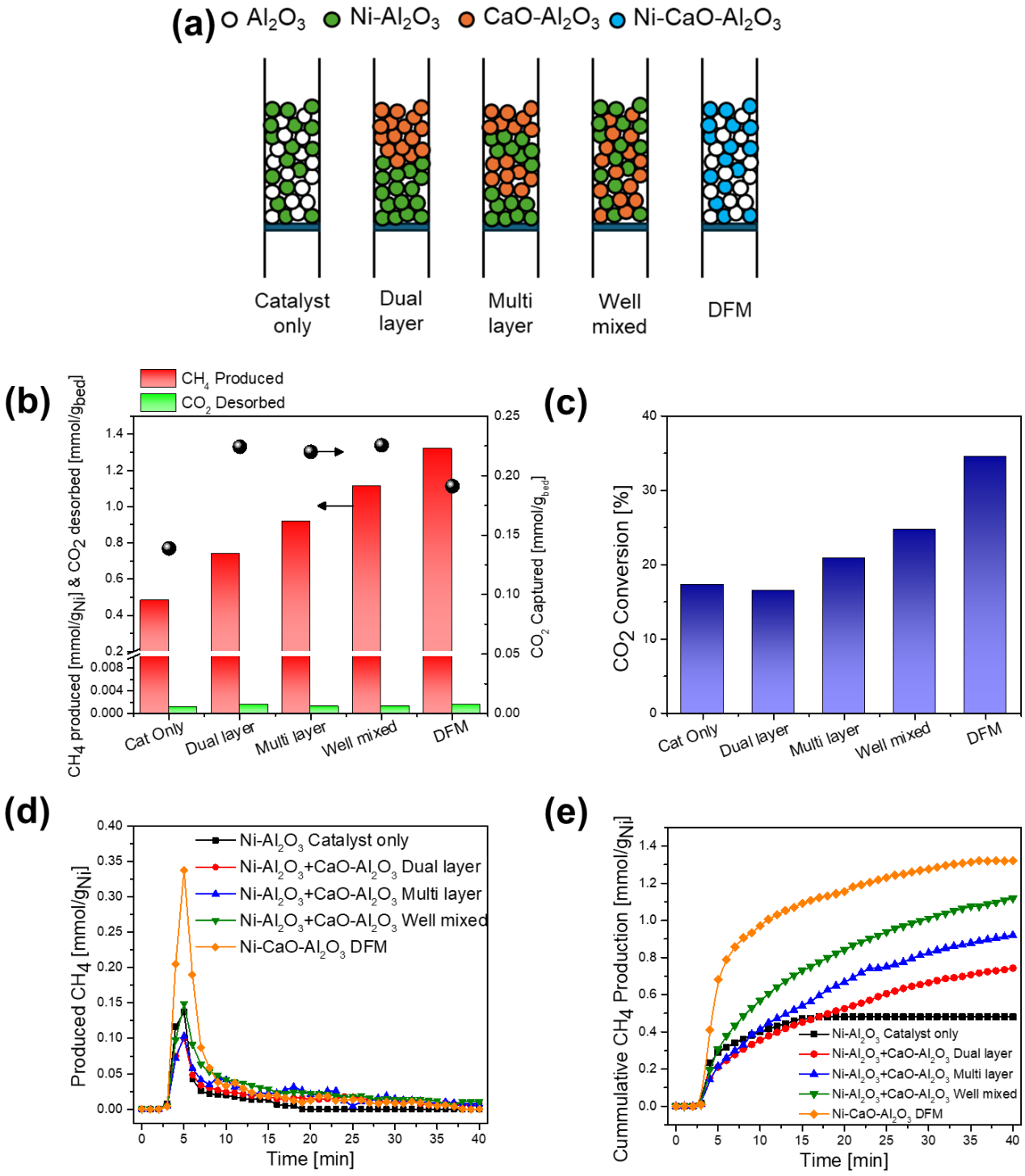

Figure 6. Integrated carbon capture methanation (ICCM) results by catalyst bed configuration: (**a**) schematic diagram of catalyst bed configuration, (**b**) CO_2 adsorption capacity, amount of produced CH_4 and desorbed CO_2 (The symbol ● represents CO_2 capture capacity (mmol/g_{bed})), (**c**) CO_2 conversion, (**d**) CH_4 production profiles in methanation step, and (**e**) cumulative CH_4 production.

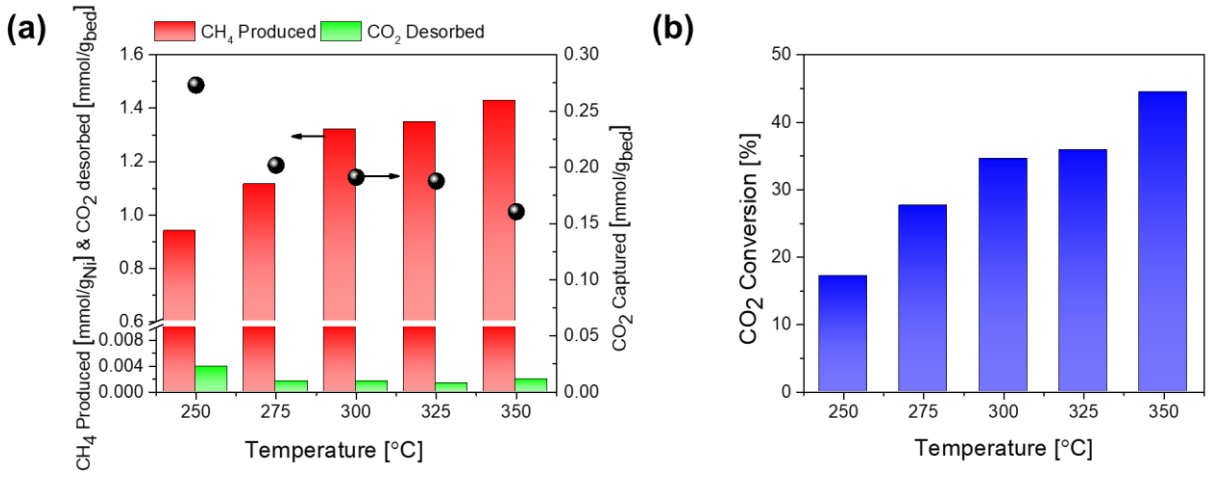

Figure 7. Integrated carbon capture methanation (ICCM) results of Ni-CaO-Al_2O_3 DFM by operation temperature: (**a**) CO_2 adsorption capacities, amount of produced CH_4 and desorbed CO_2 (The symbol ● represents CO_2 capture capacity (mmol/g_{bed})) and (**b**) CO_2 conversion.

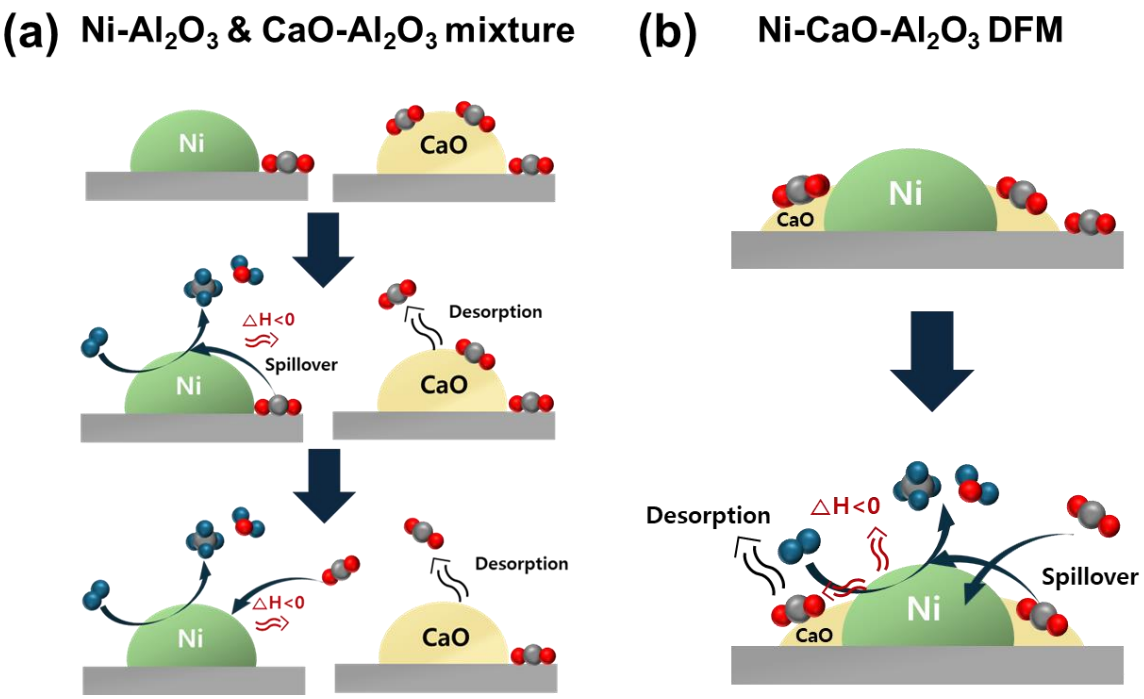

Figure 8. Schematic diagram of hydrogenation reaction pathway for (**a**) a physical mixture of catalyst and adsorbent and (**b**) the dual function material.

3. Materials and Methods

3.1. Materials

Spherical alumina supports (particle diameter = 1.0 mm) were provided by Sasol. Calcium nitrate tetrahydrate ($Ca(NO_3)_2{\cdot}4H_2O$, 97%) and nickel nitrate hexahydrate ($Ni(NO_3)_2{\cdot}6H_2O$, 97%) were obtained from Daejung Chemical Company (Siheung-si, Korea). All chemicals and supports were used as received.

3.2. Synthesis

The catalyst and CO_2 adsorbent were prepared using the sequential incipient wet impregnation method. To prepare Ni-CaO-Al_2O_3 dual functional material (DFM), an appropriate amount of nickel nitrate aqueous solution was added to the spherical alumina

supports. Any excess amount of water was evaporated in rotary evaporator. The resulting solid was then dried and calcined at 550 °C for 3 h in a muffle furnace. The obtained Ni-Al_2O_3 was additionally impregnated by calcium nitrate aqueous solution. The same impregnation, drying, and calcination process was applied. The nominal loading of Ni and CaO in the Ni-CaO-Al_2O_3 dual functional material is 10 wt%, respectively. To prepare the Ni-Al_2O_3 catalyst and CaO-Al_2O_3 adsorbent, the same procedure for dual functional material preparation was applied while excluding the calcium and nickel impregnation step, respectively. The nominal loading of Ni and CaO in Ni-Al_2O_3 and CaO-Al_2O_3 was 10 wt%, respectively.

3.3. Characterization

The textural properties of all catalysts were characterized by X-ray diffraction (XRD, Smartlab, Rigaku, Tokyo, Japan) and N_2-physisorption (Tristar II 3020, Micromeritics Instrument, Norcross, GA, USA). The elemental analysis was conducted through inductively coupled plasma optical emission spectrometry (ICP-OES, 5900 ICP-OES, Agilent technologies, Santa clara, CA, USA). All samples were digested by aqua regia before ICP-OES analysis.

The H_2-pulse chemisorption was carried out to calculate Ni metal dispersion (BELCAT II, Microtrac, York, PA, USA). Before H_2 injection, 50 mg of each sample was reduced at 800 °C for 1 h under 50 mL/min of 4% H_2/Ar stream, followed by evacuation of physically adsorbed H_2 for 1 h under inert Ar stream. After being allowed to cool to 50 °C under inert Ar stream, the H_2 pulses were injected until saturated. To calculate Ni dispersion, stoichiometry factor was assumed to be H/Ni of 1 [57].

The CO_2-TPD and H_2-TPSR tests were performed using BELCAT II (Microtrac, software version 2.5.1) equipped with TCD. Prior to CO_2-TPD measurement, 50 mg of each of the samples was reduced at 800 °C for 1 h under 4% H_2/Ar stream, then cooled to 50 °C under He stream. The adsorption of CO_2 was assessed under 20% CO_2/He for 1 h and 30 min of purge with inert He stream, followed by ramping the temperature to 900 °C at the heating rate of 10 °C/min. In H_2-TPSR measurement, 0.1 g of mixed sample (catalyst + adsorbent or alumina) was used. Prior to H_2-TPSR test, the catalyst and adsorbent mixture was reduced at 800 °C under H_2/Ar stream. After reduction, the catalyst mixture was cooled down to 300 °C, followed by CO_2 adsorption for 1 h. After being purged with Ar stream to desorb physically adsorbed CO_2 molecule, the catalyst mixture was allowed to cool to room temperature. The H_2-TPSR test was then performed by heating the sample to 900 °C with a heating rate of 10 °C/min under H_2/Ar stream.

3.4. The Catalytic Activity Test

Direct CO_2 methanation and the integrated carbon capture methanation (ICCM) test were conducted in a fixed bed quartz tube reactor (inner diameter 7 mm) at atmospheric pressure. In the direct CO_2 methanation test, 0.1 g of catalyst and adsorbent mixture was charged between quartz wool. To equalize the content of Ni and CaO in the catalyst bed, a physical mixture of the catalyst and the adsorbent (0.05 g Ni-Al_2O_3 + 0.05 g Al_2O_3, 0.05 g Ni-Al_2O_3 + 0.05 g CaO-Al_2O_3, 0.05 g Ni-CaO-Al_2O_3 + 0.05 g Al_2O_3, 0.05 g CaO-Al_2O_3 + 0.05 g Al_2O_3, 0.1 g Al_2O_3) was charged. Prior to direct methanation, the catalyst mixture was reduced at 800 °C under 90 mL/min of 50% H_2/N_2 stream for 1 h. After cooling the reactor to 200 °C, the CO_2 methanation reaction was conducted by injecting 100 mL/min of feed gas (N_2/CO_2/H_2 = 5/1/4) from 200 to 600 °C at a heating rate of 1.67 °C/min.

Before the integrated carbon capture methanation (ICCM) test, the mixture of 0.5 g of catalyst (Ni-Al_2O_3 and Ni-CaO-Al_2O_3) and 0.5 g of Al_2O_3 was charged between quartz wool. In the case of the mixture of Ni-Al_2O_3+CaO-Al_2O_3, 0.5 g of each catalyst and adsorbent was charged with three different bed configurations (dual layer, multi-layer, and well mixed). The catalyst was reduced at 800 °C under 10 mL/min of a 20% H_2/N_2 stream for 1 h, then purged with an inert N_2 stream for 30 min. When the temperature for the CO_2

capture process reached a steady state, 20 mL/min of feed gas was introduced into the catalyst bed through valve switching. The feed gas composition of CO_2 capture step was set as CO_2/N_2 = 1/1. The CO_2 capture step was performed for 10 min. After the CO_2 capture step, the catalyst bed was purged using inert N_2 stream for 10 min to evacuate physically adsorbed CO_2. Subsequently, a methanation step was conducted for 40 min by introducing 20 mL/min of a 50% H_2/N_2 stream. The CO_2 and CH_4 concentrations of the effluent gas stream from the CO_2 capture step and the methanation step were analyzed through on-line gas chromatography (YL-6500GC, Younglin instrument) equipped with TCD and carboxen 1000 packed column (SUPELCO). The CO_2 capture capacity, CH_4 produced and CO_2 desorbed were calculated as follows:

$$CO_2 \text{ capture capacity } [\text{mmol/g}] = \frac{1}{W}\int_{t_0}^{t} F_{CO_2,out,blank} - F_{CO_2,out}\, dt \quad (9)$$

$$CH_4 \text{ produced } [\text{mmol/g}] = \frac{1}{W}\int_{t_0}^{t} F_{CH_4,out}\, dt \quad (10)$$

$$CO_2 \text{ desorbed } [\text{mmol/g}] = \frac{1}{W}\int_{t_0}^{t} F_{CO_2,out}\, dt \quad (11)$$

where W and F_i are the sample weight and molar flow rate of CO_2 and CH_4, respectively.

4. Conclusions

In this study, we investigated the cooperative interaction between spillover and heat exchange by integrating a CaO adsorbent into a Ni-Al_2O_3 catalyst in ICCM system. A dual functional material (DFM) was successfully prepared by sequential wet impregnation method. CO_2-TPD revealed that the main adsorption sites of CO_2 were located on the CaO surface. H_2-TPSR analysis presents the existence of distinct main reaction pathways for Ni-CaO-Al_2O_3 DFM and Ni-Al_2O_3 + CaO-Al_2O_3 physical mixture. The fast initial methane production rate of Ni-CaO-Al_2O_3 DFM is attributed to the increased amount of adsorbed CO_2 that spilled over to metallic Ni. Moreover, the heat generated during the methanation reaction could provide the energy for the desorption of strongly adsorbed CO_2 by efficient heat transfer. The close distance of methanation sites and CO_2 adsorption sites in Ni-CaO-Al_2O_3 DFM facilitate the synergistic effect of CO_2 spillover and efficient heat transfer, resulting in enhanced methane production rate and CO_2 conversion.

Author Contributions: Conceptualization, D.S.C. and H.J.K.; methodology, D.S.C.; investigation, H.J.K.; writing—original draft preparation, D.S.C.; writing—review and editing, H.J.K.; resources, J.K.; visualization, H.Y.; supervision, J.B.J. All authors have read and agreed to the published version of the manuscript.

Funding: This work was supported by the National Research Foundation of Korea (NRF) grant funded by the Korea government (MSIT) (No. RS-2023-00259920). This work was supported in part by the Human Resources Development Program of the Korea Institute of Energy Technology Evaluation and Planning (KETEP) grant funded by the Ministry of Trade, Industry and Energy, Republic of Korea (No. RS-2023-00237035).

Data Availability Statement: The original contributions presented in the study are included in the article. Further inquiries can be directed to the corresponding author.

Conflicts of Interest: The authors declare no conflicts of interest.

References

1. Pachauri, R.K.; Allen, M.R.; Barros, V.R.; Broome, J.; Cramer, W.; Christ, R.; Church, J.A.; Clarke, L.; Dahe, Q.; Dasgupta, P. *Climate Change 2014: Synthesis Report. Contribution of Working Groups I, II and III to the Fifth Assessment Report of the Intergovernmental Panel on Climate Change*; IPCC: Geneva, Switzerland, 2014.
2. Pales, A.F.; Bennett, S. *Energy Technology Perspectives 2020*; International Energy Agency: Paris, France, 2020.

3. Chang, H.; Khan, I.; Yuan, A.; Khan, S.; Sadiq, S.; Khan, A.; Shah, S.A.; Chen, L.; Humayun, M.; Usman, M. Polyarylimide-Based COF/MOF Nanoparticle Hybrids for CO_2 Conversion, Hydrogen Generation, and Organic Pollutant Degradation. *ACS Appl. Nano Mater.* **2024**, *7*, 10451–10465. [CrossRef]
4. Khan, A.; Sadiq, S.; Khan, I.; Humayun, M.; Jiyuan, G.; Usman, M.; Khan, A.; Khan, S.; Alanazi, A.F.; Bououdina, M. Preparation of visible-light active MOFs-Perovskites (ZIF-67/$LaFeO_3$) nanocatalysts for exceptional CO_2 conversion, organic pollutants and antibiotics degradation. *Heliyon* **2024**, *10*, e27378. [CrossRef] [PubMed]
5. Zhang, F.; Zhao, P.; Niu, M.; Maddy, J. The survey of key technologies in hydrogen energy storage. *Int. J. Hydrog. Energy* **2016**, *41*, 14535–14552. [CrossRef]
6. Arsad, A.Z.; Hannan, M.A.; Al-Shetwi, A.Q.; Mansur, M.; Muttaqi, K.M.; Dong, Z.Y.; Blaabjerg, F. Hydrogen energy storage integrated hybrid renewable energy systems: A review analysis for future research directions. *Int. J. Hydrog. Energy* **2022**, *47*, 17285–17312. [CrossRef]
7. Liang, Z.; Gao, H.; Rongwong, W.; Na, Y. Comparative studies of stripper overhead vapor integration-based configurations for post-combustion CO_2 capture. *Int. J. Greenh. Gas Control* **2015**, *34*, 75–84. [CrossRef]
8. Oyenekan, B.A.; Rochelle, G.T. Alternative stripper configurations for CO_2 capture by aqueous amines. *AIChE J.* **2007**, *53*, 3144–3154. [CrossRef]
9. Erans, M.; Manovic, V.; Anthony, E.J. Calcium looping sorbents for CO_2 capture. *Appl. Energy* **2016**, *180*, 722–742. [CrossRef]
10. Lysikov, A.I.; Salanov, A.N.; Okunev, A.G. Change of CO_2 Carrying Capacity of CaO in Isothermal Recarbonation—Decomposition Cycles. *Ind. Eng. Chem. Res.* **2007**, *46*, 4633–4638. [CrossRef]
11. Arias, B.; Abanades, J.C.; Grasa, G.S. An analysis of the effect of carbonation conditions on CaO deactivation curves. *Chem. Eng. J.* **2011**, *167*, 255–261. [CrossRef]
12. Wahby, A.; Ramos-Fernández, J.M.; Martínez-Escandell, M.; Sepúlveda-Escribano, A.; Silvestre-Albero, J.; Rodríguez-Reinoso, F. High-Surface-Area Carbon Molecular Sieves for Selective CO_2 Adsorption. *ChemSusChem* **2010**, *3*, 974–981. [CrossRef]
13. Silvestre-Albero, J.; Wahby, A.; Sepúlveda-Escribano, A.; Martínez-Escandell, M.; Kaneko, K.; Rodríguez-Reinoso, F. Ultrahigh CO_2 adsorption capacity on carbon molecular sieves at room temperature. *Chem. Commun.* **2011**, *47*, 6840–6842. [CrossRef] [PubMed]
14. Sarker, A.I.; Aroonwilas, A.; Veawab, A. Equilibrium and Kinetic Behaviour of CO_2 Adsorption onto Zeolites, Carbon Molecular Sieve and Activated Carbons. *Energy Procedia* **2017**, *114*, 2450–2459. [CrossRef]
15. Lv, Z.; Ruan, J.; Tu, W.; Hu, X.; He, D.; Huang, X.; Qin, C. Integrated CO_2 capture and In-Situ methanation by efficient dual functional Li4SiO_4@Ni/CeO_2. *Sep. Purif. Technol.* **2023**, *309*, 123044. [CrossRef]
16. Sun, H.; Zhang, Y.; Guan, S.; Huang, J.; Wu, C. Direct and highly selective conversion of captured CO_2 into methane through integrated carbon capture and utilization over dual functional materials. *J. CO2 Util.* **2020**, *38*, 262–272. [CrossRef]
17. Arellano-Treviño, M.A.; Kanani, N.; Jeong-Potter, C.W.; Farrauto, R.J. Bimetallic catalysts for CO_2 capture and hydrogenation at simulated flue gas conditions. *Chem. Eng. J.* **2019**, *375*, 121953. [CrossRef]
18. Kosaka, F.; Sasayama, T.; Liu, Y.; Chen, S.-Y.; Mochizuki, T.; Matsuoka, K.; Urakawa, A.; Kuramoto, K. Direct and continuous conversion of flue gas CO_2 into green fuels using dual function materials in a circulating fluidized bed system. *Chem. Eng. J.* **2022**, *450*, 138055. [CrossRef]
19. Sun, H.; Zhang, Y.; Wang, C.; Isaacs, M.A.; Osman, A.I.; Wang, Y.; Rooney, D.; Wang, Y.; Yan, Z.; Parlett, C.M.A.; et al. Integrated carbon capture and utilization: Synergistic catalysis between highly dispersed Ni clusters and ceria oxygen vacancies. *Chem. Eng. J.* **2022**, *437*, 135394. [CrossRef]
20. Jo, S.B.; Woo, J.H.; Lee, J.H.; Kim, T.Y.; Kang, H.I.; Lee, S.C.; Kim, J.C. A novel integrated CO_2 capture and direct methanation process using Ni/CaO catal-sorbents. *Sustain. Energy Fuels* **2020**, *4*, 4679–4687. [CrossRef]
21. Bermejo-López, A.; Pereda-Ayo, B.; González-Marcos, J.A.; González-Velasco, J.R. Modeling the CO_2 capture and in situ conversion to CH_4 on dual function Ru-Na_2CO_3/Al_2O_3 catalyst. *J. CO2 Util.* **2020**, *42*, 101351. [CrossRef]
22. Jo, S.B.; Woo, J.H.; Lee, J.H.; Kim, T.Y.; Kang, H.I.; Lee, S.C.; Kim, J.C. CO_2 green technologies in CO_2 capture and direct utilization processes: Methanation, reverse water-gas shift, and dry reforming of methane. *Sustain. Energy Fuels* **2020**, *4*, 5543–5549. [CrossRef]
23. Lv, Z.; Du, H.; Xu, S.; Deng, T.; Ruan, J.; Qin, C. Techno-economic analysis on CO_2 mitigation by integrated carbon capture and methanation. *Appl. Energy* **2024**, *355*, 122242. [CrossRef]
24. Chen, L.; Chen, Y.; Wei, G.; Liu, K. Conceptual design and assessment of Integrated capture and methanation of CO_2 from flue gas using chemical-looping scheme of dual function materials. *Energy Convers. Manag.* **2024**, *299*, 117847. [CrossRef]
25. Jo, S.; Son, H.D.; Kim, T.-Y.; Woo, J.H.; Ryu, D.Y.; Kim, J.C.; Lee, S.C.; Gilliard-AbdulAziz, K.L. Ru/K_2CO_3–MgO catalytic sorbent for integrated CO_2 capture and methanation at low temperatures. *Chem. Eng. J.* **2023**, *469*, 143772. [CrossRef]
26. Cimino, S.; Cepollaro, E.M.; Lisi, L. Ageing study of Li-Ru/Al_2O_3 dual function material during the integrated CO_2 capture and methanation with SO_2-containing flue gas. *Carbon Capture Sci. Technol.* **2023**, *6*, 100096. [CrossRef]
27. Wang, S.; Schrunk, E.T.; Mahajan, H.; Farrauto, R.J. The Role of Ruthenium in CO_2 Capture and Catalytic Conversion to Fuel by Dual Function Materials (DFM). *Catalysts* **2017**, *7*, 88. [CrossRef]
28. Bermejo-López, A.; Pereda-Ayo, B.; Onrubia-Calvo, J.A.; González-Marcos, J.A.; González-Velasco, J.R. Enhancement of the CO_2 adsorption and hydrogenation to CH_4 capacity of Ru–Na–Ca/γ–Al_2O_3 dual function material by controlling the Ru calcination atmosphere. *J. Environ. Sci.* **2024**, *140*, 292–305. [CrossRef]

29. Huang, P.; Chu, J.; Fu, J.; Yu, J.; Li, S.; Guo, Y.; Zhao, C.; Liu, J. Influence of reduction conditions on the structure-activity relationships of $NaNO_3$-promoted Ni/MgO dual function materials for integrated CO_2 capture and methanation. *Chem. Eng. J.* **2023**, *467*, 143431. [CrossRef]
30. Arellano-Treviño, M.A.; He, Z.; Libby, M.C.; Farrauto, R.J. Catalysts and adsorbents for CO_2 capture and conversion with dual function materials: Limitations of Ni-containing DFMs for flue gas applications. *J. CO2 Util.* **2019**, *31*, 143–151. [CrossRef]
31. Sun, H.; Wang, J.; Zhao, J.; Shen, B.; Shi, J.; Huang, J.; Wu, C. Dual functional catalytic materials of Ni over Ce-modified CaO sorbents for integrated CO_2 capture and conversion. *Appl. Catal. B Environ.* **2019**, *244*, 63–75. [CrossRef]
32. Hu, L.; Urakawa, A. Continuous CO_2 capture and reduction in one process: CO_2 methanation over unpromoted and promoted Ni/ZrO_2. *J. CO2 Util.* **2018**, *25*, 323–329. [CrossRef]
33. Lawson, S.; Baamran, K.; Newport, K.; Garcia, E.; Jacobs, G.; Rezaei, F.; Rownaghi, A.A. Adsorption-Enhanced Bifunctional Catalysts for In Situ CO_2 Capture and Utilization in Propylene Production: A Proof-Of-Concept Study. *ACS Catal.* **2022**, *12*, 14264–14279. [CrossRef]
34. Tsiotsias, A.I.; Charisiou, N.D.; Hussien, A.G.S.; Sebastian, V.; Polychronopoulou, K.; Goula, M.A. Integrating capture and methanation of CO_2 using physical mixtures of Na-Al_2O_3 and mono-/ bimetallic (Ru)Ni/Pr-CeO_2. *Chem. Eng. J.* **2024**, *491*, 151962. [CrossRef]
35. Miguel, C.V.; Soria, M.A.; Mendes, A.; Madeira, L.M. A sorptive reactor for CO_2 capture and conversion to renewable methane. *Chem. Eng. J.* **2017**, *322*, 590–602. [CrossRef]
36. Wang, X.; Hong, Y.; Shi, H.; Szanyi, J. Kinetic modeling and transient DRIFTS–MS studies of CO_2 methanation over Ru/Al_2O_3 catalysts. *J. Catal.* **2016**, *343*, 185–195. [CrossRef]
37. Falbo, L.; Visconti, C.G.; Lietti, L.; Szanyi, J. The effect of CO on CO_2 methanation over Ru/Al_2O_3 catalysts: A combined steady-state reactivity and transient DRIFT spectroscopy study. *Appl. Catal. B Environ.* **2019**, *256*, 117791. [CrossRef]
38. Li, L.; Zhang, Y.; Feng, J.; Zhao, S.; Li, K.; Huang, Z.; Lin, H. Ni–Ca–Al Synergistic Effect in Dual-Function Materials for Integrated CO_2 Capture and Conversion. *ACS Sustain. Chem. Eng.* **2024**, *12*, 925–937. [CrossRef]
39. Jo, S.; Woo, J.H.; Nguyen, T.; Kim, J.E.; Kim, T.Y.; Ryu, H.-J.; Hwang, B.; Kim, J.C.; Lee, S.C.; Gilliard-AbdulAziz, K.L. Zr-Modified Ni/CaO Dual Function Materials (DFMs) for Direct Methanation in an Integrated CO_2 Capture and Utilization Process. *Energy Fuels* **2023**, *37*, 19680–19694. [CrossRef]
40. Proaño, L.; Tello, E.; Arellano-Trevino, M.A.; Wang, S.; Farrauto, R.J.; Cobo, M. In-situ DRIFTS study of two-step CO_2 capture and catalytic methanation over Ru,"Na_2O"/Al_2O_3 Dual Functional Material. *Appl. Surf. Sci.* **2019**, *479*, 25–30. [CrossRef]
41. Jeong-Potter, C.; Farrauto, R. Feasibility Study of Combining Direct Air Capture of CO_2 and Methanation at Isothermal Conditions with Dual Function Materials. *Appl. Catal. B Environ.* **2021**, *282*, 119416. [CrossRef]
42. Onrubia-Calvo, J.A.; Pereda-Ayo, B.; González-Marcos, J.A.; González-Velasco, J.R. Lanthanum partial substitution by basic cations in $LaNiO_3$/CeO_2 precursors to raise DFM performance for integrated CO_2 capture and methanation. *J. CO2 Util.* **2024**, *81*, 102704. [CrossRef]
43. Ma, X.; Li, X.; Cui, H.; Zhang, W.; Cheng, Z.; Zhou, Z. Metal oxide-doped Ni/CaO dual-function materials for integrated CO capture and conversion: Performance and mechanism. *AIChE J.* **2023**, *69*, e17520. [CrossRef]
44. Veselovskaya, J.V.; Parunin, P.D.; Netskina, O.V.; Okunev, A.G. A Novel Process for Renewable Methane Production: Combining Direct Air Capture by K_2CO_3/Alumina Sorbent with CO_2 Methanation over Ru/Alumina Catalyst. *Top. Catal.* **2018**, *61*, 1528–1536. [CrossRef]
45. Porta, A.; Visconti, C.G.; Castoldi, L.; Matarrese, R.; Jeong-Potter, C.; Farrauto, R.; Lietti, L. Ru-Ba synergistic effect in dual functioning materials for cyclic CO_2 capture and methanation. *Appl. Catal. B Environ.* **2021**, *283*, 119654. [CrossRef]
46. Duyar, M.S.; Treviño, M.A.A.; Farrauto, R.J. Dual function materials for CO_2 capture and conversion using renewable H_2. *Appl. Catal. B Environ.* **2015**, *168–169*, 370–376. [CrossRef]
47. Choi, D.S.; Kim, N.Y.; Yoo, E.; Kim, J.; Joo, J.B. Enhanced coke resistant Ni/SiO_2@SiO_2 core–shell nanostructured catalysts for dry reforming of methane: Effect of metal-support interaction and SiO_2 shell. *Chem. Eng. Sci.* **2024**, *299*, 120480. [CrossRef]
48. Hu, J.; Hongmanorom, P.; Galvita, V.V.; Li, Z.; Kawi, S. Bifunctional Ni-Ca based material for integrated CO_2 capture and conversion via calcium-looping dry reforming. *Appl. Catal. B Environ.* **2021**, *284*, 119734. [CrossRef]
49. Das, S.; Ashok, J.; Bian, Z.; Dewangan, N.; Wai, M.H.; Du, Y.; Borgna, A.; Hidajat, K.; Kawi, S. Silica–Ceria sandwiched Ni core–shell catalyst for low temperature dry reforming of biogas: Coke resistance and mechanistic insights. *Appl. Catal. B Environ.* **2018**, *230*, 220–236. [CrossRef]
50. Huynh, H.L.; Zhu, J.; Zhang, G.; Shen, Y.; Tucho, W.M.; Ding, Y.; Yu, Z. Promoting effect of Fe on supported Ni catalysts in CO_2 methanation by in situ DRIFTS and DFT study. *J. Catal.* **2020**, *392*, 266–277. [CrossRef]
51. Bartos, B.; Freund, H.J.; Kuhlenbeck, H.; Neumann, M.; Lindner, H.; Müller, K. Adsorption and reaction of CO_2 and CO_2/O CO-adsorption on Ni(110): Angle resolved photoemission (ARUPS) and electron energy loss (HREELS) studies. *Surf. Sci.* **1987**, *179*, 59–89. [CrossRef]
52. Schreiter, N.; Kirchner, J.; Kureti, S. A DRIFTS and TPD study on the methanation of CO_2 on Ni/Al_2O_3 catalyst. *Catal. Commun.* **2020**, *140*, 105988. [CrossRef]
53. Sasayama, T.; Kosaka, F.; Liu, Y.; Yamaguchi, T.; Chen, S.-Y.; Mochizuki, T.; Urakawa, A.; Kuramoto, K. Integrated CO_2 capture and selective conversion to syngas using transition-metal-free Na/Al_2O_3 dual-function material. *J. CO2 Util.* **2022**, *60*, 102049. [CrossRef]

54. Zheng, Q.; Farrauto, R.; Chau Nguyen, A. Adsorption and Methanation of Flue Gas CO_2 with Dual Functional Catalytic Materials: A Parametric Study. *Ind. Eng. Chem. Res.* **2016**, *55*, 6768–6776. [CrossRef]
55. Duyar, M.S.; Wang, S.; Arellano-Treviño, M.A.; Farrauto, R.J. CO_2 utilization with a novel dual function material (DFM) for capture and catalytic conversion to synthetic natural gas: An update. *J. CO2 Util.* **2016**, *15*, 65–71. [CrossRef]
56. Zhou, Y.; Ma, X.; Yusanjan, Q.; Cui, H.; Cheng, Z.; Zhou, Z. Active metal-free CaO-based dual-function materials for integrated CO_2 capture and reverse water–gas shift. *Chem. Eng. J.* **2024**, *485*, 149937. [CrossRef]
57. Gallego-García, D.; Iriarte-Velasco, U.; Gutiérrez-Ortiz, M.A.; Ayastuy, J.L. Nickel aluminate spinel-derived catalysts for aqueous-phase hydrogenolysis of glycerol with in-situ hydrogen production: Effect of molybdenum doping. *Appl. Catal. B Environ. Energy* **2024**, *344*, 123671. [CrossRef]